# BRAIN COMMUNICATIONS

# Whole-brain dynamical modelling for classification of Parkinson's disease

©Kyesam Jung, <sup>1,2</sup> ©Esther Florin, <sup>3</sup> ©Kaustubh R. Patil, <sup>1,2</sup> Julian Caspers, <sup>4</sup> Christian Rubbert, <sup>4</sup> ©Simon B. Eickhoff <sup>1,2</sup> and ©Oleksandr V. Popovych <sup>1,2</sup>

Simulated whole-brain connectomes demonstrate enhanced inter-individual variability depending on the data processing and model-ling approach. By considering the human brain connectome as an individualized attribute, we investigate how empirical and simulated whole-brain connectome-derived features can be utilized to classify patients with Parkinson's disease against healthy controls in light of varying data processing and model validation. To this end, we applied simulated blood oxygenation level-dependent signals derived by a whole-brain dynamical model simulating electrical signals of neuronal populations to reveal differences between patients and controls. In addition to the widely used model validation via fitting the dynamical model to empirical neuroimaging data, we invented a model validation against behavioural data, such as subject classes, which we refer to as behavioural model fitting and show that it can be beneficial for Parkinsonian patient classification. Furthermore, the results of machine learning reported in this study also demonstrated that the performance of the patient classification can be improved when the empirical data are complemented by the simulation results. We also showed that the temporal filtering of blood oxygenation level-dependent signals influences the prediction results, where filtering in the low-frequency band is advisable for Parkinsonian patient classification. In addition, composing the feature space of empirical and simulated data from multiple brain parcellation schemes provided complementary features that improved prediction performance. Based on our findings, we suggest that combining the simulation results with empirical data is effective for inter-individual research and its clinical application.

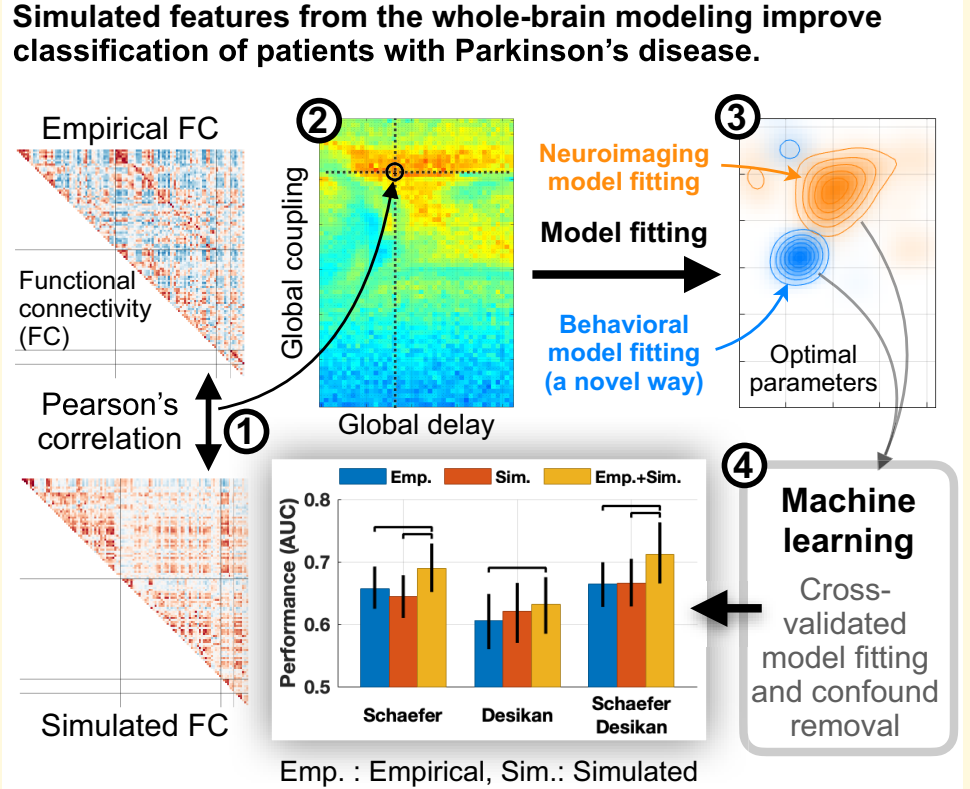
- 1 Institute of Neuroscience and Medicine, Brain and Behaviour (INM-7), Research Centre Jülich, 52425 Jülich, Germany
- 2 Institute for Systems Neuroscience, Medical Faculty, Heinrich-Heine University Düsseldorf, 40225 Düsseldorf, Germany
- 3 Institute of Clinical Neuroscience and Medical Psychology, Medical Faculty, Heinrich-Heine University Düsseldorf, 40225 Düsseldorf, Germany
- 4 Department of Diagnostic and Interventional Radiology, Medical Faculty, Heinrich-Heine University Dusseldorf, 40225 Düsseldorf, Germany

Correspondence to: Oleksandr V. Popovych Institute of Neuroscience and Medicine Brain and Behaviour (INM-7) Research Centre Jülich, 52425 Jülich, Germany E-mail: o.popovych@fz-juelich.de

Keywords: whole-brain simulation; MRI; Parkinson's disease; patient classification; machine learning

**Abbreviations:** AUC = area under a curve; BF = broad-frequency band; BOLD = blood oxygenation level-dependent; BW = Balloon–Windkessel; CV = cross-validation; DWI = diffusion-weighted image; EPSP = excitatory postsynaptic potential; FC = functional connectivity; FOD = fibre oriented distribution; GoF = goodness-of-fit; HC = healthy control; HF = high-frequency band; IPSP = inhibitory postsynaptic potential; LASSO = least absolute shrinkage and selection operator; LF = low-frequency band; NF = no filtering; PD = Parkinson's disease; PL = path length; PSP = postsynaptic potential; ROC = receiver operating characteristic; SC = streamline count; T<sub>1</sub>w = T<sub>1</sub>-weighted image; WBT = whole-brain tractography

#### **Graphical Abstract**



- A low-frequency band-pass filtering (from 0.01 to 0.05 Hz) for blood oxygenation level-dependent (BOLD) signals is advisable.
- Simulated data from multiple brain parcellation schemes provide complementary features for patient classification.

#### Introduction

For decades, large-scale whole-brain connectivity acquired from non-invasive *in-vivo* MRI has actively been used to study the human brain as an integrative complex system.<sup>1</sup> Accordingly, anatomical (or structural) and functional connectivities between brain regions have been used. Previous studies have shown that the structural architecture shapes the temporal synchronization between the blood oxygenation level-dependent (BOLD) signals in selected networks, for instance the default mode network.<sup>2,3</sup> However, the structure-function correspondence is not high for whole-brain connectivity.<sup>4-6</sup> The correspondences between the brain connectomes of the same and different subjects, samples or data modalities<sup>7,8</sup> have been considered to investigate the inter-individual differences<sup>9</sup> or diagnostic classification between healthy controls (HCs) and patients.<sup>4,10-12</sup>

Connectivity relationships are also commonly used when brain dynamics are modelled by mathematical whole-brain dynamical models. In particular, finding the strongest

correspondence (the highest similarity) between empirical functional connectivity (eFC) and simulated functional connectivity (sFC) has been used for model validation. <sup>13–15</sup> Such a correspondence of the simulated data to the empirical data may undergo qualitative changes when parameters of a given model vary and the validation procedure consists in finding the most pronounced agreement between the data and the model fitted by searching for optimal parameter points.

Previous studies utilizing the discussed whole-brain modelling showed that the employed modelling approach was applicable to clinical research. The variability of the model parameters between diseased and healthy states has been investigated for brain disorders including schizophrenia, <sup>16–19</sup> Alzheimer's disease, <sup>20</sup> Parkinson's disease <sup>21,22</sup> and stroke patients. <sup>23</sup> For instance, Saenger *et al.* <sup>22</sup> showed that therapeutic deep brain stimulation in Parkinson's disease can be modelled by the normal form of a Hopf bifurcation model. <sup>24</sup> Detailed simulations of neuronal dynamics may also provide a way to test prognostic outcomes *in silico* throughout virtual operations and optimize the setup and parameters of therapeutic interventions. <sup>25–28</sup>

There are, however, no well-established standards for model validation against empirical data. Several fitting modalities have been suggested in the literature, including the fitting of the grand-averaged empirical and simulated FC matrices, fitting the dynamical FCs, maximization of the metastability and structure-functional model fitting. 6,13,24,29,30 On that account, it is necessary to investigate, which parameter points of a given dynamical mode and which model fitting modalities are the most suitable to answer a given research question by the modelling approach. For example, it was observed that the distributions of the optimal model parameters differ when using only functional or structure-functional model fitting and may lead to subject stratifications showing different model fitting values and optimal parameter points.<sup>30</sup> It is also well known that varying parameters of MRI data processing influence the empirical structural and functional connectomes and their analyses.<sup>31–34</sup> This subsequently affects model validation.<sup>6,30,35</sup> Therefore, the impact of data processing on the results of model validation should be carefully considered, especially in clinical applications.

In Parkinson's disease research, the eFC of the restingstate networks was already being used in machine learning approaches to subject classification. 36,37 When sFC is involved, it is essential to extract relevant features for Parkinson's disease classification from simulation results via searching in a given model parameter space for the optimal model. To do this, we considered two aspects of parameters regarding dynamical models and data processing. First, we find the model parameters that reveal the most prominent differences in connectome correspondence between Parkinson's disease and HC. Such an approach can be used for model validation. Here, we aim at a diagnostic classification of patients from healthy subjects, where the model fitting to behavioural (phenotypical) data might be an alternative approach for model validation. We attempt to provide a way to reveal and maximize the group difference in simulated results by varying the parameters of dynamical models. For instance, the disease status of the subjects can be used for behavioural fitting, as we show in this study. Second, we consider different temporal filters of BOLD signals, which are known to influence FC properties. 38,39 In particular, the altered frequency bands were found to retain Parkinson's disease-related neural changes. 40 The frequencies of empirical BOLD signals, when included in the wholebrain mathematical models, may influence the optimal model parameters and the quality of the model fitting.<sup>6,30</sup> In this context, investigation of the impact of temporal filtering conditions on the model validation in Parkinson's disease data is important.

In the current study, we advance the classification of clinical data by application of machine learning to empirical and simulated connectomes. The functional connectomes were calculated from empirical and simulated BOLD signals, respectively, filtered in broad-, low- and high-frequency bands for two different brain parcellations as given by the Schaefer<sup>41</sup> and Desikan–Killiany<sup>42</sup> brain atlases. As compared with purely empirical studies, we take the next step

based on the two aspects of parameters for model fitting modality and data processing and employ the simulated data to improve the prediction results in a machine learning setting.

The current study employs whole-brain dynamical modelling of the resting-state functional MRI data based on the Jansen-Rit model type of interacting excitatory and inhibitory neuronal populations. 43,44 The simulated FCs generated for the optimal model parameters based on model fitting modalities were used to calculate the connectome relationships (Pearson's correlation) with empirical structural and functional connectivities. We also introduced a simple but effective method for model validation against behavioural data more suitable for differentiation between patients with Parkinson's disease and HCs than the conventionally used model fit to neuroimaging data. Consequently, the personalized features derived from the connectome relationships were used in this study for classification of Parkinson's disease and HC using machine learning. We in particular show that complementing empirical data with simulated FC can improve the prediction performance for unseen subjects. Our results suggest that the personalized whole-brain models can serve as an additional source of information relevant for disease diagnosis and possibly for their treatment as well.

#### Materials and methods

We performed three main steps to obtain the whole-brain connectivities eFC, eSC (empirical streamline counts), ePL (empirical average path length) and sFC. Figure 1 schematically illustrates the data processing and simulation workflow. We applied four temporal filtering conditions to empirical and simulated resting-state BOLD signals. Subsequently, we considered three types of connectivity relationship corresponding to the correlation between eFC and eSC, the correlation between eSC and sFC and the correlation between eFC and sFC. Since sFC was calculated by varying the two free model parameters of global coupling and global delay, the correlations involving sFC change, as illustrated by the eFC-sFC correlation landscape in the parameter space in Fig. 1 (the rightmost colour plot). We used these three connectivity relationships as features for the Parkinson's disease classification via a machine learning approach. To this end, we trained Parkinson's disease classifiers and evaluated their performance based on prediction probabilities obtained on unseen subjects.

#### Subjects and demography

The three considered whole-brain connectivities (eFC, eSC and sFC) were calculated for 51 (30 males) HC and 65 (45 males) patients with Parkinson's disease, see Table 1 for the demography. Patients and controls were included in an MRI data pool acquired at the University Hospital Düsseldorf, Germany, which was also used in several recent studies, <sup>36,37,45,46</sup> where additional details about the data

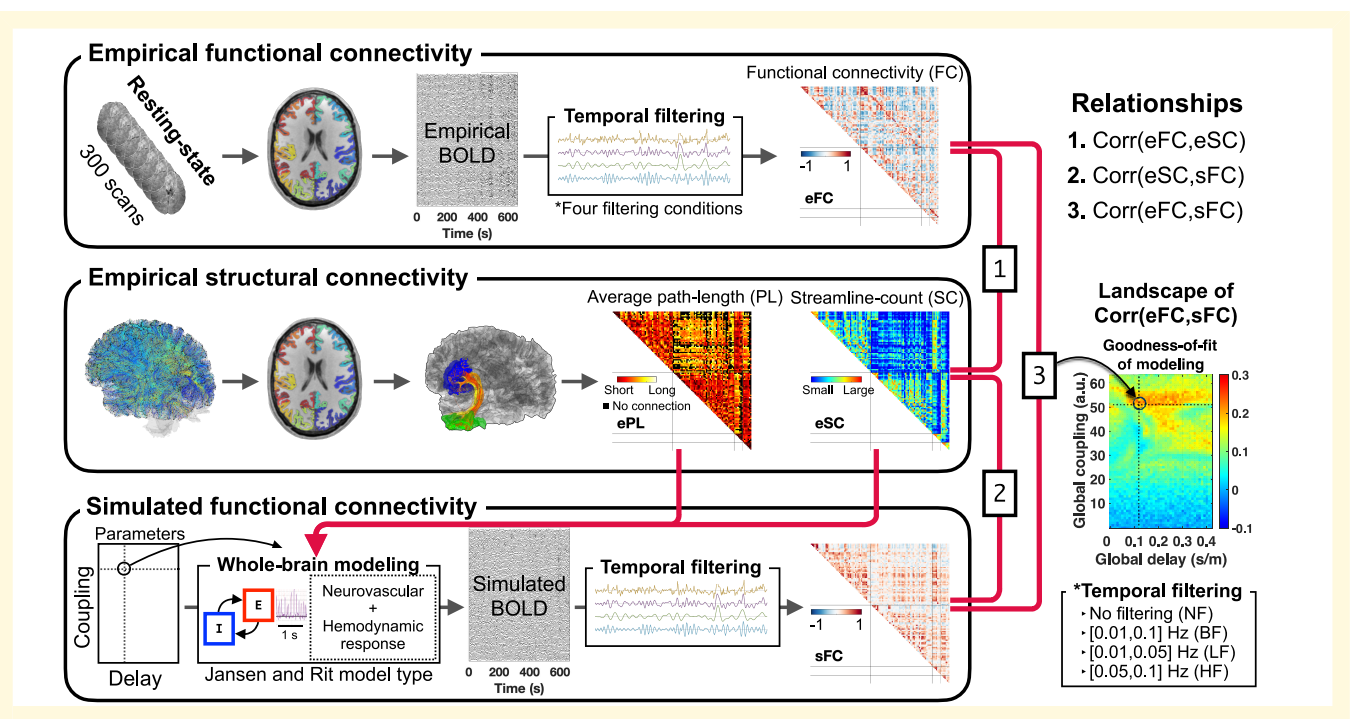


**Figure 1 Data processing and simulation overview.** First (upper box), brain parcellations in the native space of T<sub>1</sub>w were prepared and applied to the processed functional MRI data, BOLD signals were extracted from the corresponding brain regions and filtered according to four temporal filtering conditions (right *bottom* box) and four respective eFCs were calculated. Second (*middle* box), the parcellations were also used for the calculation of the structural connectivity by extracting streamlines from the WBT reconstructed using DWIs, where the number and length of streamlines connecting any two brain regions were collected into matrices of eSC and ePL. Third (lower box), the structural connectome (eSC and ePL) was used to build a brain network for the whole-brain modelling that simulates BOLD signals, which were filtered according to the considered filtering conditions (right *bottom* box) and used to calculate sFC. Subsequently, we calculated connectivity relationships (Pearson's correlation) using these three connectivity matrices: (i) corr (eFC, eSC); (ii) corr (sFC, eSC); and (ii) corr (eFC, sFC). Model parameters for global coupling and global delay were varied to validate the model against empirical data. In particular, the correspondence (correlation) between eSC and eFC and sFC was calculated for each parameter point, resulting in similarity landscapes in the model parameter space, see the example of the relationship between eFC and sFC in the rightmost colour plot. The most pronounced correspondence (correlation) between the empirical and simulated connectomes was selected, together with the respective optimal model parameters, as a result of the neuroimaging model fitting for further analysis.

Table | Demography of subjects included in the study

Groups	Mean (standard	deviation) years	years Statistical tests	
	All subjects		χ <sup>2</sup> goodness-of-fit test	
All	58.93 (10.25)		I 16 subjects	0.149
	HC	Patients	Wilcoxon rank-sum two-tail test	
All	55.02 (9.69)	62.00 (9.62)	51 HC versus 65 patients	0.000
Female	56.52 (9.40)	60.80 (8.96)	21 HC versus 20 patients	0.201
Male	53.97 (9.74)	62.53 (9.85)	30 HC versus 45 patients	0.001
	Females	Males	Wilcoxon rank-sum two-tail test	
All	58.61 (9.43)	59.11 (10.67)	41 females versus 75 males	0.751

can be found. All patients were diagnosed with Parkinson's disease by an experienced movement disorder specialist. All HC subjects had no history of any neurological or psychiatric disease and no abnormalities were detected in cranial MRI. The ages of 116 subjects (mean: 58.9 years and standard deviation: 10.3 years) are in a normal distribution (the null hypothesis was not rejected by a  $\chi^2$  goodness-of-fit test with P = 0.15). The age of patients was significantly higher

than that of controls (Wilcoxon rank-sum two-tail test). The age of male patients was significantly higher than that of male controls, but the age of females was not from distributions with different medians. There was no age difference between females and males (Table 1). The study was approved by the local ethics committee and performed in accordance with the Declaration of Helsinki. All subjects provided written informed consent prior to study inclusion.

#### MRI acquisition

Structural and functional MRI data were acquired using a 3 T scanner (Siemens Trio). A structural brain image was acquired using a 3D  $T_1$ -weighted image ( $T_1$ w) sequence (TR = 2.3 s, TE = 2.96 ms, TI = 900 ms, flip-angle = 9°, field-of-view =  $240 \times 256 \text{ mm}^2$  in sagittal, the number of slices = 160, voxel dimension =  $240 \times 256 \times 160$ , voxel size =  $1.0 \times 1.0 \times 1.1$ mm<sup>3</sup>). Diffusion-weighted images (DWI) comprised a single non-weighted (B<sub>0</sub>) image and weighted (B =  $1000 \text{ s/mm}^2$ ) images with 64 directions (TR = 6.7 s, TE = 81 ms, phase encoding: anterior to posterior, field-of-view =  $216 \times 216 \text{ mm}^2$ in axial, the number of slices = 55, voxel dimension =  $90 \times$  $90 \times 55$ , voxel size =  $2.4 \times 2.4 \times 2.4$  mm<sup>3</sup>). Resting-state functional MRI was obtained using an echo-planar imaging sequence during 663 s (TR = 2.21 s, TE = 30 ms, field-of-view  $=200\times200$  mm<sup>2</sup> in axial, the number of slices = 36, voxel dimension =  $64 \times 64 \times 36$ , voxel size =  $3.125 \times 3.125 \times 3.565$ mm<sup>3</sup>). To prevent the distraction of streamline tracking, artefact volumes of DWI were removed from the data based on evaluation by two raters.

#### **Preprocessing of MRI**

For the personalized data processing, we developed a containerized in-house pipeline to process structural and functional MRI in the native spaces. The pipeline consists of five modules: preprocessing of structural MRI (T<sub>1</sub>w and DWI), wholebrain tractography (WBT) calculation, atlas transformation, reconstruction of structural connectivity (eSC and ePL) and preprocessing of functional MRI. The pipeline comprises Freesurfer, <sup>47</sup> FSL, <sup>48</sup> ANTs, <sup>49</sup> MRtrix3<sup>50</sup> and AFNI. <sup>51</sup> It is publicly available (https://jugit.fz-juelich.de/inm7/public/vbcmri-pipeline).

The preprocessing module of structural MRI performed the following steps: bias-field correction for T<sub>1</sub>w, alignment of anterior-posterior commissures of T<sub>1</sub>w, recon-all by Freesurfer, removing the Gibbs ringing artefacts of DWIs, bias-field correction for DWIs, corrections of head motion, b-vector rotations and eddy distortion of DWIs and co-registration between averaged DWI and T<sub>1</sub>w. This module segmented subcortical areas based on voxel intensities of the T<sub>1</sub>w. It also prepared labelling annotations using a brain atlas, for which a classifier was available from the literature. The annotation can also be created based on a subject cohort by capturing region data either drawn by neuroanatomists or according to dedicated algorithms.<sup>52</sup>

The WBT calculation module included only MRtrix3 functions. They estimated response functions for spherical deconvolution using the constrained deconvolution algorithm.<sup>53</sup> Fibre oriented distributions (FODs) were estimated from the DWIs using spherical deconvolution, and the WBT was created through the fibre tracking by the second-order integration over the FOD by a probabilistic algorithm.<sup>54</sup> In the latter step, we used 10 million total streamlines for the WBT density. The tracking parameters of the tckgen function were set as in the previous study:<sup>30</sup>

step size = 0.625 mm, angle =  $45^{\circ}$ , minimal length = 2.5 mm, maximal length = 250 mm, FOD amplitude for terminating tract = 0.06, maximum attempts per seed = 50, the maximum number of sampling trials = 1000 and downsampling = 3 (FOD samples per steps−1).

The atlas transformation module annotated labels using a classifier to parcel cortical regions in the native T<sub>1</sub>w space using Freesurfer. In the present study, we applied two atlas classifiers for brain parcellations, the Schaefer atlas with 100 parcels<sup>41</sup> and the Desikan–Killiany atlas with 68 parcels. 42 Both atlases provide cortical parcellations, where the former is based on functional MRI data, while the latter is labelled by gyral-based anatomical parcellation. After this, the subcortical areas segmented by the preprocessing module were included and combined with the labelled cortical parcels. Finally, the pipeline transformed the labelled image (cortical parcels and subcortical regions) from the  $T_1$ w to DWI native spaces.

The reconstruction module calculated the matrices of the streamline counts (SCs) and the matrices of the average path lengths (PLs) of the streamlines extracted between any two parcellated brain regions from the calculated WBT with the transformed, labelled image in the DWI space.

The preprocessing module of functional MRI performed slice time correction, head motion correction, re-slicing in a 2 mm iso-cubic voxel space, intensity normalization, detrending with filtering of very slow fluctuations out (high pass), co-registration to the T<sub>1</sub>w and calculation of regressors for the white matter, cerebrospinal fluid (CSF) and brain global signals as well as for the head motion. The pipeline also transformed the labelled image of the brain parcellation generated in the native T<sub>1</sub>w space to the functional MRI native space. Finally, we performed a nuisance regression with the prepared regressors (white matter, CSF and the brain global signals, as well as head motions).

#### Post-processing of functional MRI

After preprocessing of MRI, we extracted mean BOLD signals based on the annotated atlas labels and applied three temporal band-pass filtering conditions in the frequency ranges of (0.01,0.1) Hz (broad-frequency band; BF), (0.01,0.05) Hz (low-frequency band; LF) and (0.05,0.1) Hz (high-frequency band; HF). Therefore, four filtering conditions were considered: no filtering (NF), BF, LF and HF. The filtering was done using a script in the Python programming language (version 3.8, Python Software Foundation, https://www.python.org/) using the SciPy (version 1.5) signal processing module<sup>55</sup> and NumPy<sup>56</sup> (version 1.19) for the temporal band-pass filtering. We used the Butterworth digital filter of order 6, scipy.signal.butter.

#### Whole-brain model

#### Convolution-based two-population model for electrical signals

The whole-brain resting-state dynamics considered in this study was simulated by a system of N coupled neuronal

models representing the mean brain regional activity. Each region contains two populations for each neuronal type (excitatory and inhibitory) that interact with each other via postsynaptic potentials (PSPs). The considered convolution-based model is of the Jansen–Rit type 44,57 and simulates the PSP signals involving other brain regions that interact with time delay in coupling according to the calculated structural connectivity, i.e. SC and PL matrices. The following set of differential equations describes the mean dynamics of the excitatory and inhibitory PSPs of region n = 1, 2, ..., N,

$$\dot{y}_{n,e}(t) = z_{n,e}(t),\tag{1}$$

$$\dot{y}_{n,i}(t) = z_{n,i}(t),\tag{2}$$

$$\dot{z}_{n,e}(t) = P_{n,e}(t) - 2aR_n z_{n,e}(t) - a^2 R_n^2 y_{n,e}(t) + \eta_{n,e}, \quad (3)$$

$$\dot{z}_{n,i}(t) = P_{n,i}(t) - 2bR_n z_{n,i}(t) - b^2 R_n^2 y_{n,i}(t) + \eta_{n,i},$$

$$n = 1, 2, \dots, N.$$
(4)

Here,  $z_{n,e}$ ,  $z_{n,i}$ ,  $y_{n,e}$  and  $y_{n,i}$  are the excitatory postsynaptic current, the inhibitory postsynaptic current, the excitatory PSP (EPSP) and the inhibitory PSP (IPSP) of the brain region n, respectively, where the subscripts e and i stand for excitatory and inhibitory, accordingly. The model (1)–(4) is a system of driven harmonic oscillators in a critical damping regime, where the system quickly returns to its steady state after perturbation without undershooting. Parameters a and b represent the reciprocal of the time constants of the PSP kernel for the two populations for EPSP and IPSP, respectively.  $\eta_{n,e}$  and  $\eta_{n,i}$  are independent noise sampled from a random uniform distribution between -1.5 and  $1.5 \text{ V/s}^2$ . For frequency of oscillations, we also introduced a scaling factor R. By increasing R, the spectral power of the PSP signals shifts to higher frequencies. Perturbation  $P_{n,e}$  drives EPSP oscillations regarding input signals from other regions, i.e. it models the coupling between the network nodes/brain regions and  $P_{n,i}$  perturbs IPSP oscillations by the input from the excitatory population in the same region n,

$$P_{n,e}(t) = AaR_n^2 \sigma_e \left( \frac{C}{N} \sum_{m \neq n}^{N} C_{nm} y_{m,e}(t - \tau_{nm}) - C_{ei} y_{n,i}(t) \right), \quad (5)$$

$$P_{n,i}(t) = BbR_n^2 \sigma_i(C_{ie} \gamma_{n,e}(t)), \quad n = 1, 2, \dots, N.$$
 (6)

A and B are the maximum amplitudes of the PSP kernels for EPSP and IPSP, respectively. N is the total number of brain regions/network nodes for the whole-brain model. In Equation (5), C is a global coupling parameter, which scales the couplings throughout the whole-brain network.  $C_{nm}$  is the strength of the individual coupling from region m to region n, which is realized via weighting the EPSP signal of the m-th network node  $y_{m,e}$  considered with time delay  $\tau_{nm}$ . Parameter  $C_{ei}$  weights an input coming from the inhibitory population of the same brain region, i.e. IPSP  $y_{n,i}$ . The

individual time delays and coupling strengths between regions m and n can be estimated from the empirical data as

$$\tau_{nm} = \tau_{global} L_{nm}, \ C_{nm} = \frac{w_{nm}}{W}, \tag{7}$$

where the averaged path length  $L_{nm}$  (from the matrix PL) of the reconstructed streamlines between regions n and m is scaled by a global delay parameter  $\tau_{global}$ .  $C_{nm}$  in Equation (7) calculates an individual coupling strength by taking into account the SC matrix, where the number of streamlines  $w_{nm}$  between the two regions was normalized by an averaged number of streamlines W calculated over all connections except for the self-connections. As follows from Equation (5), the coupling between brain regions is realized between the excitatory populations, where the delayed EPSP signals from the other brain regions composed the coupling term. Together with the intra-regional coupling by the IPSP signal from the inhibitory population, the total PSP input to the excitatory population is converted by a nonlinear sigmoid function  $\sigma_e(v)$  given in Equation (8) below to an averaged firing density. The inhibitory population in region n received an input EPSP signal weighted by parameter  $C_{ie}$  from the excitatory population of the same region only, which was again converted to an averaged firing density by the following sigmoid function  $\sigma_i(v)$ :

$$\sigma_e(\nu) = \frac{F_e}{1 + e^{r(\nu_0 - \nu)}}, \ \sigma_i(\nu) = \frac{F_i}{1 + e^{r(\nu_0 - \nu)}}.$$
 (8)

In Equation (8) of the mentioned sigmoid functions, the parameter r is a slope,  $v_0$  is a half of the maximal neural activity and parameters  $F_e$  and  $F_i$  are the maximal firing densities of the excitatory and inhibitory populations, respectively. Parameter values of the considered two-population model Equations (1)–(8) are given in Table 2.

#### **Simulated BOLD signals**

We calculated the regional BOLD signals using the corresponding EPSP signals simulated by the electrical model Equations (1)–(8) introduced in the previous section. Several examples of the time courses of the EPSP signals generated by the considered model and their power spectra are illustrated in Supplementary Fig. 1. Neurovascular coupling and hemodynamic responses constitute the process reflected in the Balloon–Windkessel (BW) model that was utilized to convert the simulated neural activity to BOLD signals, <sup>58–60</sup> see details in the Supplementary material.

# Model validation: neuroimaging and behavioural model fitting

In this study, we considered two model fitting approaches: neuroimaging model fitting and behavioural model fitting. The former is well known in the literature and consists of validation of the model via comparing simulated data against neuroimaging empirical data. In this study, the Pearson's

Table 2 Parameter values of the electrical model and the BW model

Electrical model	Variables	Values	BW model	Variables	Values
Max. sigmoid (excitatory)	$F_{e}$	$100 \ s^{-1}$	Echo time	TE	30 ms
Reciprocal of the time constant of the EPSP kernel	а	$100^{a} \text{ s}^{-1}$	Mean-transit-time	t <sub>MTT</sub>	2 <sup>b</sup> s
Max. EPSP	Α	3.25° mV	Net oxygen extraction fraction at rest	Eo	0.4 <sup>b</sup>
Max. sigmoid (inhibitory)	$F_i$	50 s <sup>-1</sup>	Venous blood volume fraction	V <sub>o</sub>	4 <sup>b</sup> %
Reciprocal of the time constant of the IPSP kernel	Ь	$50^{a} \text{ s}^{-1}$	Frequency offset for 3 T	$g_0$	$80.6^{b} s^{-1}$
Max. IPSP	В	22 <sup>a</sup> mV	Ratio of intra/extra-vascular signal	ε	0.3 <sup>b</sup>
Slope of sigmoid	r	$0.56^{a} \text{ mV}^{-1}$	Sensitivity (regression slope)	$r_0$	25 <sup>b</sup> s <sup>-1</sup>
50% neural activity	<b>v</b> <sub>0</sub>	6ª mV	Steady state flow-volume relationship	α	0.38 <sup>b</sup>
Intra-regional coupling	Cie	6	Rate constant for damped oscillations	κ	0.64 <sup>b</sup> Hz
(from excitatory to inhibitory)			·		
Intra-regional coupling	$C_{ei}$	6	Rate constant for damped oscillations	γ	0.32 <sup>b</sup> Hz
(from inhibitory to excitatory)			•	,	
Scaling factor	R	2.2	Values of initial conditions	[s, f, v, q]	[0,1,1,1] <sup>c</sup>
Amplitude of noise		1.5 V/s <sup>2</sup>			

aValues from Jansen and Rit study.44

bValues from Havlicek et al. 58

cValues empirically determined based on the trajectories generated by the BW model.

EPSP, excitatory postsynaptic potential; IPSP, inhibitory postsynaptic potential.

correlation coefficient between eFC and sFC (comparing the upper triangle without self-connections of the connectivity matrices) was calculated and denoted as goodness-of-fit (GoF) values. Searching for the maximal GoF in a given parameter space is a well-established approach for model validation in whole-brain modelling studies. 13-15 In this study, we optimized the coupling and delay model parameters to maximize the GoF value on a parameter grid of 64 × 43 points (64 global couplings and 43 global delays) densely covering the parameter plane, respectively. In addition, we also considered the connectivity relationship between eSC and sFC as for separate neuroimaging model fitting. In consequence, two types of neuroimaging model fitting (eFC versus sFC and eSC versus sFC) were used in this study. As this procedure fits the model to the connectivity derived from the empirical neuroimaging data, we term it neuroimaging model fitting.

We also introduce behavioural model fitting as a procedure to validate a model against behavioural data, for example, optimizing the model to reflect some behavioural (phenotypical) properties to the best possible extent. In this study, we optimized the parameters of the model to maximally differentiate between Parkinson's disease patients and HC subjects. For this, we calculated the effect size based on the z-statistics of the Wilcoxon rank-sum two-tail test as given by the Rosenthal formula, i.e. the normal z-statistics divided by the square root of the number of observations<sup>61</sup> of the difference between the (neuroimaging) GoF values of the HC and Parkinson's disease subject groups. The effect size was calculated for every parameter point in the considered parameter space of 64 × 43 grid and represented as a parameter map. In this way we obtained a parameter landscape of the group differences and were able to investigate the differentiation of GoF values of Parkinson's disease patients from those of HC subjects. This parameter landscape reflects the relation of the model GoF to the behavioural

data (in this study, to the differentiation based on clinical measures), and we thus used this approach as behavioural model fitting. To evaluate the parameter areas of significant group difference, we performed the Wilcoxon rank-sum two-tail test and obtained a corresponding P-value parameter map. Due to the multiple comparisons over the parameter points, we applied the random-field thresholding scheme <sup>62,63</sup> using a 2D Gaussian kernel smoothing. Subsequently, we obtained a Z-score map and thresholded it to retain statistically significant parameter areas (alpha = 0.05). Finally, we searched for the optimal model parameters within the significant parameter areas corresponding to the maximal effect size. We considered two connectivity relationships (eFC versus sFC and eSC versus sFC) for the behavioural model fitting.

## Random sampling for optimal parameters

We performed a random sampling to test the stability of the optimal parameter points for the behavioural model fitting. To do this, the stability of the results was assessed by sexbalanced stratified subsampling. After a random sampling of 72 subjects (36 HC subjects and 36 Parkinson's disease patients) out of 116 subjects, we applied the behavioural model fitting to the sampled subjects and found optimal parameters corresponding to the largest effect size. The subsampling and the corresponding calculations were repeated 1000 times.

# Regularized (least absolute shrinkage and selection operator) logistic regression

The current task is to train a binary classifier (Parkinson's disease versus HC) using 10 features (five connectivity

relationships from two parcellation schemes), which are of lower dimension than observations (116 subjects). We considered a simple regularized logistic regression that is a sparse method possessing good interpretability and is known to work well in many applications. 64-66 There might be other methods that could give better accuracy.<sup>67</sup> The main goal of the current study was however to compare the prediction results between several computational conditions including data processing and model validation. This could be demonstrated using such a linear (interpretable) machine learning method without an exhaustive search for the methods and conditions for the best performance. Thus, logistic regression is applicable to the current study. To this end, we used a regularized logistic regression with the least absolute shrinkage and selection operator (LASSO) for training and classification of HC versus Parkinson's disease subjects.<sup>68</sup> To avoid an overfit, the training error included the deviance and an L<sub>1</sub>-penalty.<sup>69</sup> We used the lassoglm function for the logistic LASSO regression and the glmval function for predicted probability calculation in the Statistics and Machine Learning Toolbox of MATLAB R2020b.

# Confound regression for age-controlled features

We used a cross-validation (CV) scheme to train the logistic LASSO regression for Parkinson's disease classification. As for a degenerative disease, <sup>70,71</sup> features for Parkinson's disease classification should be controlled by an age effect via a confound regression. Due to a random sampling from the same cohort and the usage of the same data for model validation and model training, it is important to prevent possible data leakage during the CV procedure, especially for behavioural model fitting as it uses data across subjects. Otherwise, the trained models might be biassed due to the usage of the results of the behavioural model fitting derived from Parkinson's disease classification against HC. In this respect, we followed the ideas of the cross-validated confound regression<sup>72</sup> as illustrated in Fig. 2. Specifically, we applied the CV-consistent approach to features derived from the empirical result, neuroimaging and behavioural model fitting. Accordingly, the subjects were split into training and test sets (Fig. 2, green and orange blocks in the outer loop) and the optimal parameter point of the behavioural model fitting was calculated on the training set at every iteration of the outer CV loop (Fig. 2, the green box with the Circle 1). Then the respective connectome relationships were calculated for every subject. Next, the age was regressed out for these subjects (cross-validated confound regressions in Fig. 2, Circles 1 and 2) from the obtained features of connectivity relationships used for subject classification. The optimal model parameters and the regression coefficients obtained for the training set were then used for the connectome calculation and the age regression for the test subjects.

#### **Nested cross-validation**

In order to avoid over-optimistic results of CV, 73 we used nested CV to train the logistic LASSO regression for Parkinson's disease classification (Fig. 2). In the outer loop, we randomly split the subjects into five subsets. One subset of 20% of subjects was considered as a test set (unseen subjects, the orange box in the outer loop in Fig. 2) and the other four subsets were pulled together and composed a training set (the green boxes in the outer loop in Fig. 2). As explained above, we first applied the cross-validated model fitting and confound regression to the features in the training set (Fig. 2, the green box with the Circle 1). Subsequently, the training set (age-controlled) was split into ten subsets for the nested CV in the inner loop. A logistic LASSO regression model was trained with the hyperparameters minimizing the 10-fold CV error. This model was then applied to predict the test set. As follows from the aforementioned, the agecontrolled training and test sets were used for model training and prediction, respectively. The training and testing procedure we performed can be summarized as follows:

- (i) Randomly split the entire subject cohort into five subgroups.
- (ii) Select one group as a test set and compound the others into a training set.
- (iii) Perform the cross-validated (behavioural) model fitting using the training set and extract respective connectome relationships corresponding to the optimal model parameters.
- (iv) Perform the cross-validated confound (age) regression for the training set from the features based on the connectome relationships used for classification.
- (v) Train the logistic LASSO regression model in the inner loop with a 10-fold CV that minimizes errors in the prediction model.
- (vi) Apply the trained best model to predict the test set with age regression, where the optimal model parameters of the model fitting and age regression coefficients obtained for the training set were used (Fig. 2, the dashed arrow in the outer loop).
- (vii) Calculate the model performance using a confusion matrix and an receiver operating characteristic (ROC) curve.
- (viii) Perform Steps (ii)–(vii) for the other four subsets split in Step (i) as test sets in the outer CV loop (five prediction results).
- (ix) Repeat Steps (i)–(viii), 50 times (250 prediction results in total).

#### **Evaluation of prediction performance**

For Parkinson's disease classification based on the discussed machine learning approach, we considered five features for each of the two parcellation schemes (Schaefer and Desikan–Killiany atlases), i.e. 10 features in total: corr (eFC, eSC) as an empirical feature, corr (eFC, sFC) and corr (eSC, sFC) as simulated features for each model fitting,

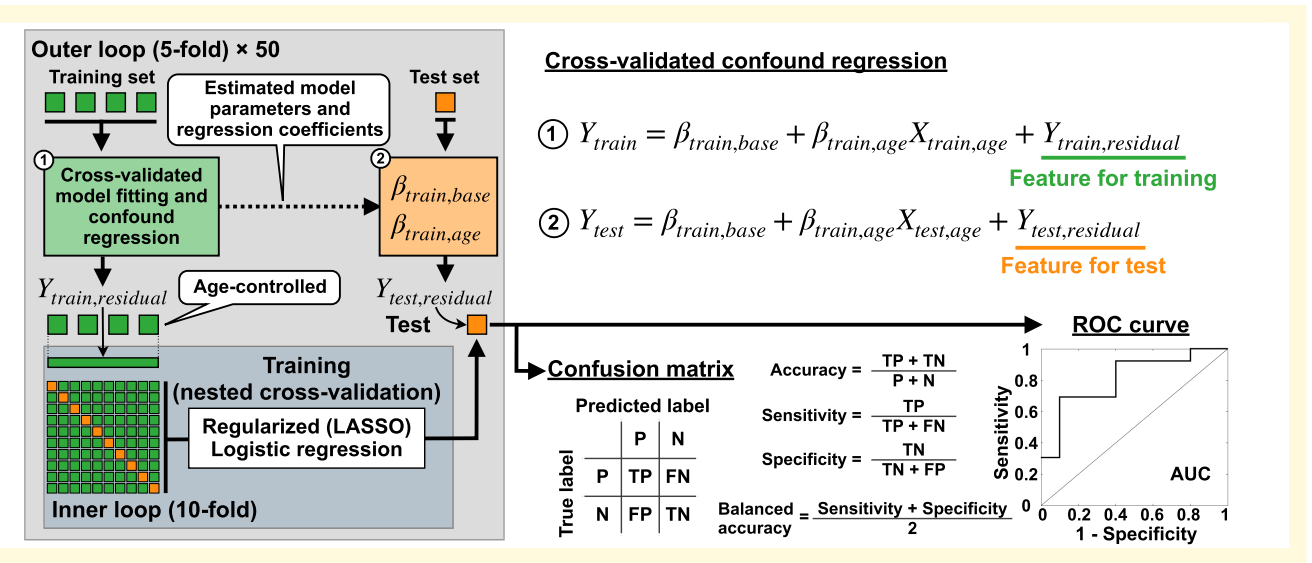


**Figure 2 Schematic illustration of cross-validated model fitting, cross-validated confound regression and nested CV.** The boxes under the 'Training set' in the leftmost plot illustrate randomly split subject subgroups used for training the model in the 5-fold outer loop and in the 10-fold inner loop. The box under the 'Test set' in the outer loop depicts the testing subject subgroup used for evaluation of the prediction performance of the trained model as given by accuracy, sensitivity, specificity, balanced accuracy and area under the ROC curve. *P*, positive as patients; N, negative as controls; TP, true positive; FP, false positive; TN, true negative; FN, false negative.

i.e. the neuroimaging model fitting and the behavioural model fitting. To investigate the impact of simulated results on the Parkinson's disease prediction, we composed the considered features into three conditions: (i) empirical features only (shuffle simulated features); (ii) simulated features only (shuffle empirical features); and (iii) all features (no shuffling). The shuffling was performed by a random redistribution of the values of a given feature among subjects such that the correspondence of the feature to individual subjects was destroyed. By focusing on some features (connectome relationships and parcellations), the other features were shuffled. For example, to focus on the empirical features of the Schaefer atlas, four simulated features (eFC versus sFC and eSC versus sFC for two model fitting modalities) of the Schaefer atlas and all five features (one empirical and four simulated features) of the Desikan-Killiany atlas were shuffled. The shuffling was performed for every feature separately, randomizing feature values across subjects while retaining distributional properties (Supplementary Fig. 2). After feature selection, model training and application of the trained model to the unseen test subject set, we calculated a confusion matrix from the prediction results and plotted a ROC curve.<sup>74</sup> The latter was calculated from the prediction results obtained by varying the subject classification threshold of a predicted probability from 0 to 1. Then, we calculated the prediction performance (accuracy, sensitivity, specificity and balanced accuracy) and the area under a curve (AUC) of the ROC curve.

In addition to the prediction considering the cross-validated confound regression with subjects' ages using the entire cohort, we also applied the same approach to a balanced subject configuration by excluding the 17 oldest

Parkinson's disease patients from 116 subjects. Thus, the balanced cohort has no significant age difference between Parkinson's disease and HC groups with balanced group sizes (see Supplementary Table 1). Subsequently, we analysed the prediction performances of the balanced subject cohort (99 subjects).

#### Statistical analysis

Statistical analysis was performed using functions in the Statistics and Machine Learning Toolbox of MATLAB R2020b. We set significance level at P < 0.05. We applied the Bonferroni correction to prevent multiple comparison issues when the test was used multiple times. Statistical tests used in the results were mentioned in each legend of figures and tables. We also scrutinized the prediction probabilities for individual subjects to evaluate the model's performance. Here, the trained model estimated the predicted probabilities for each subject in the test set. Subsequently, we calculated a fraction of actual positives and showed relationships using probability calibration. The ideal case is to have the same values for the fraction of positives and the predicted probability, i.e. the graph should align to the diagonal. In clinical applications, the tight correspondence between predicted probabilities and the fraction of actual positives provides high trustworthiness for diagnosis.<sup>75</sup> To this end, we used the Brier score<sup>76</sup> to calculate the mean-squared error of each predicted probability against an ideal case. We also used the Wasserstein distance to show how much cost is required to turn a given distribution of the predicted probabilities into a uniform one.<sup>77</sup> In other words, this metric was used to evaluate how well predicted probabilities were uniformly distributed. Thus, a lower Wasserstein distance means that the predicted probabilities are relatively better calibrated than those of a higher one. Accordingly, we further evaluated the model's performance regarding individual predicted probabilities in addition to the integrative performance from the confusion matrix.

#### Results

In this study, we investigated the application of simulation results from whole-brain dynamical models to Parkinson's disease classification using relationships between empirical and simulated connectomes as features. The whole-brain dynamical model of the Jansen–Rit type was used to simulate the electrical neuronal activity and was validated against empirical data by means of neuroimaging or behavioural model fitting. Accordingly, we calculated the connectome relationships involving the simulated connectomes corresponding to the optimal model parameters of the two fitting modalities and used them as features for Parkinson's disease classification. We show that complementing the empirical data by simulated data improves the prediction performance as compared with the case where only empirical data were used.

### **Neuroimaging model fitting**

We calculated sFC using simulated BOLD signals for each parameter point and obtained the similarity (Pearson's correlation) values between eFC and sFC. Figure 3 shows the corresponding landscapes of the GoF values in the delaycoupling  $(\tau_{global}, C)$  parameter space averaged over all subjects, the distributions of the maximal GoF values and corresponding optimal model parameters for individual subjects for the Schaefer atlas (Fig. 3A-D) and the Desikan-Killiany atlas (Fig. 3E-H). We calculated eFC and sFC for the different frequency ranges of the corresponding filtered BOLD signals, i.e. NF, BF, LF and HF conditions (see Materials and methods for details). The profiles of the parameter landscapes were different between the considered brain atlases. The Schaefer atlas showed a unimodal distribution containing maximal GoF values (the dashed circle in Fig. 3A) for the optimal global delays in the biologically feasible range<sup>78</sup> from 0.06 to 0.25 s/m (Fig. 3D). On the other hand, the maximal GoF for the Desikan-Killiany atlas posited a bi-modal distribution (the dashed circles in Fig. 3E) with well-separated peaks along the global coupling parameter (Fig. 3G, compare with Fig. 3C). Moreover, stronger global coupling of the maximal GoF values was accompanied by a widespread global delay (the upper dashed circle in Fig. 3E) that may get out of the biologically feasible range as compared with the weaker global couplings (the lower dashed circle in Fig. 3E).

Furthermore, we observed that applying temporal filtering to BOLD signals diminished GoF values over the entire parameter landscape (Fig. 3B and F). In particular, the narrow frequency bands (LF and HF) resulted in significantly lower

maximal GoF values than in the cases of the broader (BF) or entire frequency (NF) range; see Table 3 for statistical results.

# Effect size of group comparisons for behavioural model fitting

The behavioural model fitting resulted in effect sizes of group difference between HC and Parkinson's disease (Fig. 4A–B for eFC-sFC correlation, see Supplementary Fig. 3 for eSC-sFC correlation). Furthermore, we also observed that the distributions of the optimal parameter points corresponding to the maximal effect sizes are densely concentrated in the parameter space across repeated subsampling (1000 times) and filtering conditions (Fig. 4C–D, distributions in blue). Interestingly, the distributions of the optimal parameters derived from the behavioural model fitting were strikingly different from those determined by the neuroimaging model fitting (Fig. 4C–D, distributions in orange for the neuroimaging and in blue for the behavioural fitting). Both sets of optimal parameters are located in the biologically plausible range of time delay.<sup>78</sup>

# **Group difference between healthy controls and patients**

The empirical structure-function relationships corr(eFC, eSC) for HC and Parkinson's disease subject groups were found to be from distributions with different medians for the Schaefer atlas and all considered filtering conditions and for the LF condition only for the Desikan–Killiany atlas (Fig. 5, the first row). The group differences obtained by involving the simulated connectomes in the neuroimaging model fitting were small and non-significant for both atlases and all filtering conditions (Fig. 5, the second and third rows). On the other hand, for behavioural model fitting, we observed that Parkinson's disease patients exhibited stronger agreements between empirical and simulated connectomes than HC subjects and can thus be better differentiated from HC (Fig. 5, the fourth and fifth rows).

Temporal filtering may influence the group differences for the empirical and also for the simulated connectomes as illustrated in Fig. 5, see the first row for the Desikan–Killiany atlas, in particular and Supplementary Fig. 4. In addition, we calculated the explained variances of the five connectivity relationships between each other for the same and different filtering conditions, which resulted in relatively low similarities for the simulated results (Supplementary Fig. 5). Accordingly, the temporal filtering can influence the considered connectivity relationships and may lead to dissimilar patterns of connectome relationships across subjects.

#### **Prediction performance**

We used the five whole-brain connectivity relationships as features for Parkinson's disease classification using machine learning based on the logistic LASSO regression algorithm.

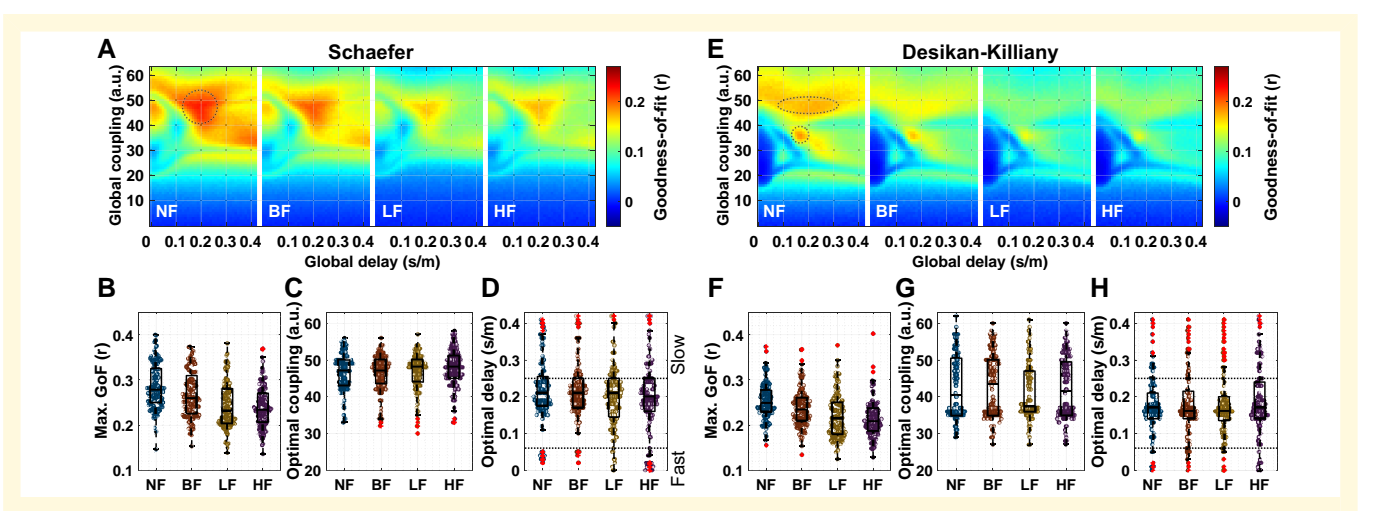


Figure 3 Results of the neuroimaging model fitting. (A–D) The Schaefer atlas and (E–H) the Desikan–Killiany atlas. (A, E) Parameter landscapes of the similarity (Pearson's correlation) between eFC and sFC, i.e. goodness-of-fit (GoF) values averaged over the entire subject cohort. The landscapes are illustrated for each filtering condition (NF, BF, LF and HF, see Materials and methods for details). The dashed circles delineate the hills with large GoF values. Distributions of (B, F) the maximal GoF values, (C, G) optimal coupling parameters and (D, H) the respective optimal delays corresponding to the maximal GoF values for each filtering condition. The distributions of the maximal GoF values are significantly different across filtering conditions (P = 0.000 for the Schaefer atlas and P = 0.000 for the Desikan–Killiany atlas; Kruskal–Wallis non-parametric one-way analysis of variance test). Post-hoc: Significantly different filtering conditions are NF > BF, NF > LF, NF > HF, BF > LF and BF > HF in both atlas conditions (Wilcoxon signed-rank two-tail test, Bonferroni corrected P < 0.05, see Table 3 for details). The distributions of the optimal coupling parameters are not significantly different (P = 0.317 for the Schaefer atlas and P = 0.505 for the Desikan–Killiany atlas; the Kruskal–Wallis test). The distributions of the optimal delays are not significantly different (P = 0.459 for the Schaefer atlas and P = 0.824 for the Desikan–Killiany atlas; the Kruskal–Wallis test). The dashed horizontal lines in plots (D, H) indicate the biologically feasible delay range regarding the electrophysiological conduction speed. The middle lines in interquartile box plots indicate the medians of distributions, and the red plus signs are the outliers.

The feature space constituted three feature conditions with ten features (five connectivity relationships for two atlases), see Supplementary Fig. 2. After the nested CV, the trained best models were relatively well balanced, with a slight tendency towards overfitting for some of the used performance measures (13.4% decreased balanced accuracy and 1.1% decreased AUC of test performance from training one, see Supplementary Fig. 6).

Figure 6 shows the prediction performance for each of the investigated conditional cases of brain parcellations, frequency bands and feature conditions. The first important observation is that involvement of the simulated connectomes can improve the classification of Parkinson's disease and HC, see Fig. 6 and compare blue dots (empirical features) to red dots (simulated features) and to yellow dots (all features) (see Supplementary Fig. 7 for the differences). In the latter case, where the empirical features are complemented by the simulated ones, the prediction performance can only be enhanced as compared with purely empirical features, which we observed for most feature conditions and performance measures (Fig. 6A–C). Interestingly, the performance further improved when using features from both atlases (Fig. 6 and Supplementary Fig. 7).

We also investigated how the prediction performance varies depending on the filtering conditions (Fig. 6D). The effect of the temporal filtering was prominent of the empirical features for the Schaefer atlas, where the performance was significantly increased for the LF condition compared with the

others (Fig. 6D, the 'Emp.' column for the Schaefer atlas). On the other hand, the HF condition showed low performances on the empirical features, in particular, with very low specificities down to zero (Fig. 6B and D) and very high sensitivities up to 1 (Supplementary Fig. 8), where the LF filtering seems again to be a beneficial condition for Parkinson's disease prediction. Summarizing, the temporal filtering conditions influenced the model performance and the LF band-pass filtering resulted in the most effective prediction relying on the connectome relationships. The other considered narrow-band HF filtering condition is not advisable for Parkinson's disease classification. However, involving the simulated connectomes is still of advantage also under this condition as compared with using only empirical features.

We also compared the prediction performance when the simulated connectomes obtained from the neuroimaging and behavioural model fittings were considered separately. This resulted in two additional feature conditions (see Supplementary Fig. 8). The neuroimaging model fitting in most cases led to a weaker prediction performance compared with the behavioural model fitting or to the composite case when the features of both fittings are merged. This justifies the introduction of the behavioural model fitting for subject classification.

Furthermore, we applied the current approach to the balanced subject configuration (99 subjects, see Supplementary Table 1 for the demography). The prediction performance

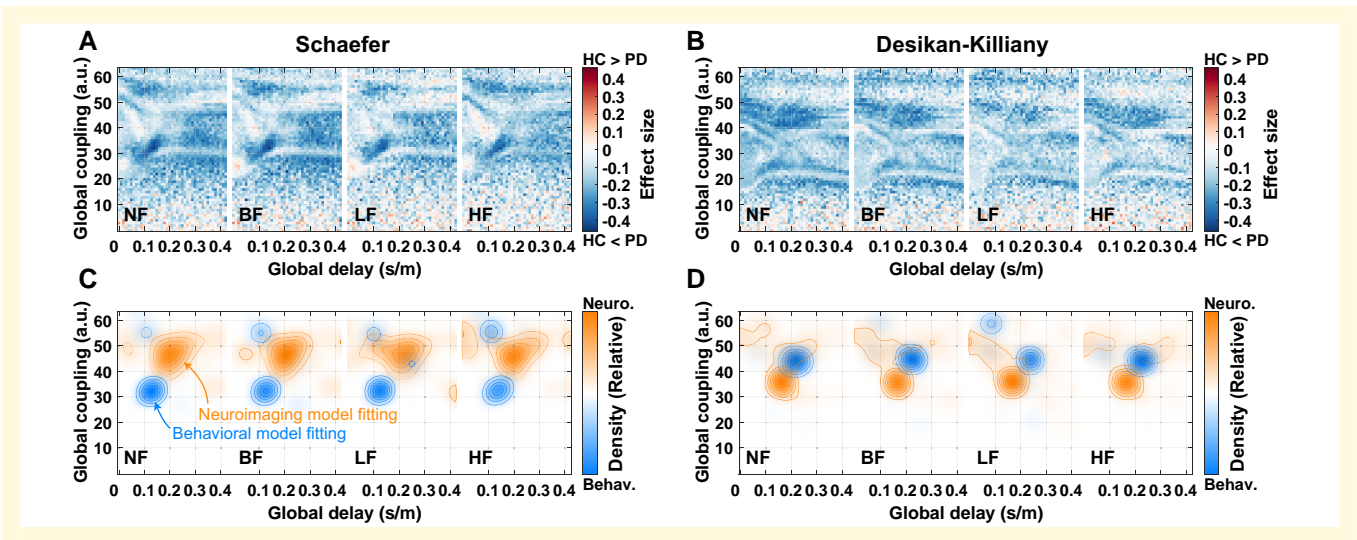


Figure 4 Parameter maps of the effect size of the difference between goodness-of-fit (GoF) values (eFC-sFC correlation) of healthy and Parkinsonian groups used for the behavioural model fitting. The filtering conditions are indicated in the plots for (A) the Schaefer atlas and (B) the Desikan–Killiany atlas. Effect sizes in the ( $\tau_{global}$ , C)-parameter plane were calculated by a non-parametric Wilcoxon rank-sum two-tailed test between patients and controls in the GoF values for each parameter point. (C, D) Distributions of optimal parameters derived from the neuroimaging model fitting (orange, all subjects, n = 116) and the behavioural model fitting (blue, repeated subsampling, n = 1000) for (C) the Schaefer atlas and (D) the Desikan–Killiany atlas.



Figure 5 Differentiation between healthy and Parkinsonian subjects as reflected by the relationships between empirical and simulated connectomes. (Left) The Schaefer atlas and (Right) the Desikan–Killiany atlas. The simulated connectomes are calculated for the optimal model parameters of the neuroimaging and behavioural model fitting as indicated on the vertical axis. Summary tables of the effect sizes (numbers) of the differences between Parkinsonian and healthy subject groups are calculated by the Rosenthal formula and shown in negative for HC < Parkinson's disease and positive for HC > Parkinson's disease. The significant cases are indicated by rectangles as given by the Bonferroni corrected *P*-values of the Wilcoxon rank-sum two-tail test.

was consistent with the main findings of the entire cohort (116 subjects, Fig. 6). In other words, complementing empirical data with simulated results using LF filtering involving multiparcellation (concatenating both atlases) is advisable for Parkinson's disease classification (Supplementary Fig. 9).

Figure 6 shows the well-known measures characterizing the prediction performance as median values and interquartile ranges of distributions. Although these measures clearly reflect how well the machine learning approach is commonly working, we may also be interested in how every test is performing for the classification of individual unseen subjects. In this respect, Fig. 7 illustrates the results of classification/prediction probabilities of all tests performed on individual

subjects from the test sets. The prediction probabilities were collected and related to the probability calibration curves.

We can interpret the probability calibration plots (Fig. 7A–C) according to two aspects. Feature conditions using simulated results (red and yellow curves) resulted in predictions that are more closely aligned with the ideal case (the diagonal black line) than the empirical relationship. Indeed, for the Schaefer atlas and the multi-parcellation case, the distance to the diagonal as given by the mean-squared error of the predicted probabilities against the actual classes calculated according to the Brier score<sup>76</sup> is minimal for the composed features, including the empirical and simulated

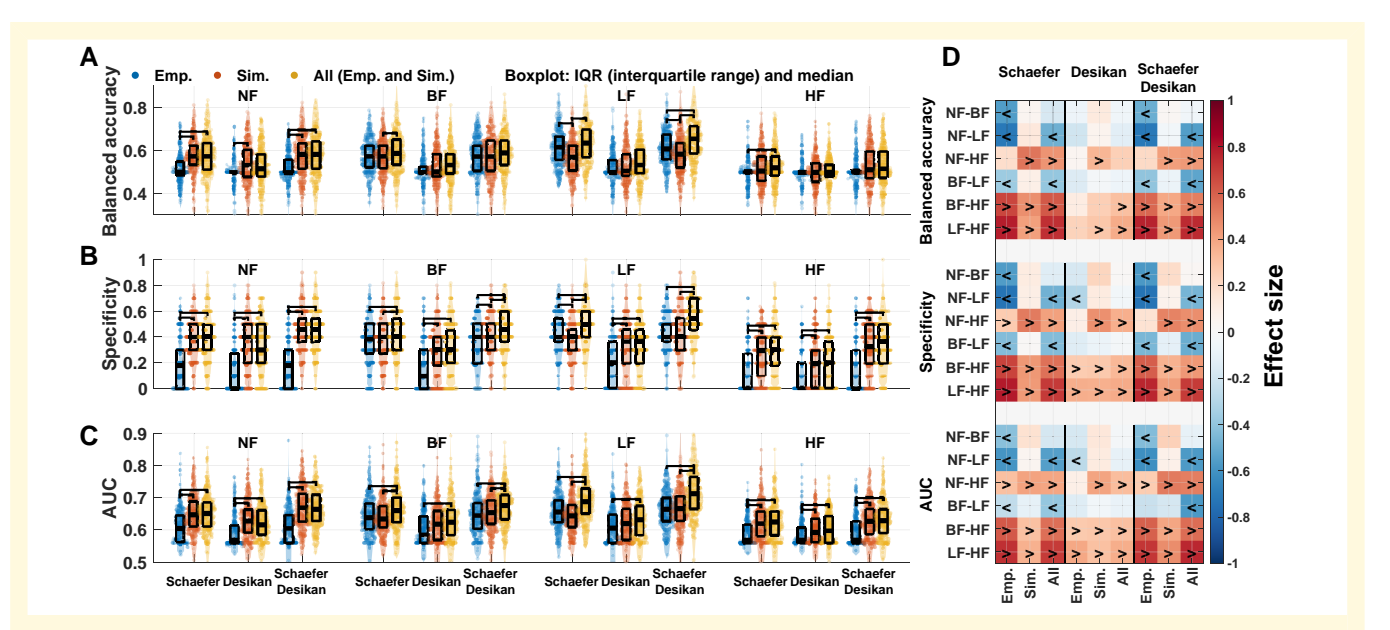


Figure 6 Summary of the performance of Parkinson's disease classification using the three different feature conditions: empirical features (left distribution), simulated features (middle distribution) and all features (right distribution) after incorporating the age controlling and the behavioural model fitting during the nested CV (Fig. 2). The median values of the balanced accuracy, specificity and AUC of the ROC curves for all considered parcellations and filtering conditions are shown in each panel for (A) balanced accuracy and (B) specificity and (C) AUC. The error bars indicate the interquartile range of 250 tests represented as data points in the plots across 50 iterations of the outer loop (5-fold) of the nested CV procedure (Fig. 2). The horizontal brackets connecting two coloured distributions indicate significantly different performance between feature conditions (Bonferroni corrected P < 0.05; Wilcoxon signed-rank two-tail test). (D) Effect sizes between filtering conditions for each feature condition. The signs '<' and '>' indicate which condition is significantly larger than the other. For example, '<' sign for 'NF-LF' indicated on the vertical axes means NF < LF for a given feature condition indicated on the horizontal axes. The Wilcoxon signed-rank two-tail test was used for comparisons across feature and filtering conditions (Bonferroni corrected statistics). The Desikan–Killiany atlas is shortend as 'Desikan'.

connectomes for the LF filtering condition (Fig. 7E). As a second aspect, the prediction probabilities derived from the empirical features are more narrowly distributed around 0.5 (blue curves in Fig. 7D) compared with the case of all features (yellow curves in Fig. 7D). This can be quantified by the minimum cost of turning the observed distribution into a uniform distribution using the Wasserstein distance (Fig. 7F). In the latter case, the predicted probabilities derived from all features show widely spreading distribution that also reach the low and high probability values, which indicates high confidence.<sup>75</sup> In other words, in our predictive modelling, the prediction results, where the empirical data were complemented by simulated features, were better calibrated in some cases as compared with the case of the empirical data only (Fig. 7C). As mentioned above, the Wasserstein distance in Fig. 7F clearly shows which filtering condition and which feature condition can be the best beneficial configuration for Parkinson's disease classification. In particular, the LF filtering of the BOLD signals and involving of the simulated connectomes together with the empirical ones for the Schaefer atlas and multi-parcellation case can improve the prediction results and the confidence of the prediction model. The same conclusion was drawn above based on the Brier scores, which confirm their robustness and may be relevant for the application of the discussed modelling and prediction approaches to clinical data and disease diagnosis.

### **Discussion**

The main objective of this study is to effectively apply wholebrain dynamical modelling and the derived simulated connectomes to Parkinson's disease classification. Whole-brain simulations allow us to explore various regimes of brain dynamics corresponding to different values of free model parameters. To extract features from the simulated results, it is essential to evaluate which model fitting is appropriate. The detected optimal model parameters can differ when we use different model fitting approaches. In other words, whole-brain dynamics with proper model parameters can disclose group differences between Parkinson's disease and HC subjects and provide a way to extract effective features for Parkinson's disease classification. In this study, we introduced the behavioural model fitting approach and showed that it captured differences between Parkinson's disease and HC better than the conventionally used neuroimaging model fitting approach. Then, we applied it to Parkinson's disease classification. Based on our findings, we can conclude that using proper model validation in whole-brain dynamical modelling may provide effective features to machine learning and provide information complementary to empirical features.

In addition to whole-brain dynamical modelling for classification, data processing is also important because, as we have shown, different data processing influences model

Table 3 Comparisons between goodness-of-fit values of the considered filtering conditions (Bonferroni corrected P-values of the Wilcoxon signed-rank two-tail test) and the corresponding effect sizes by Rosenthal formula<sup>61</sup>

P (effect size)	NF versus BF	NF versus LF	NF versus HF	BF versus LF	BF versus HF	LF versus HF
Schaefer	0.000 (0.70)	0.000 (0.84)	0.000 (0.86)	0.000 (0.81)	0.000 (0.70)	0.998 (0.04)
Desikan-Killiany	0.000 (0.66)	0.000 (0.77)	0.000 (0.85)	0.000 (0.69)	0.000 (0.70)	0.838 (0.10)

Bold fonts indicate that the goodness-of-fit values are significantly different between filtering conditions.

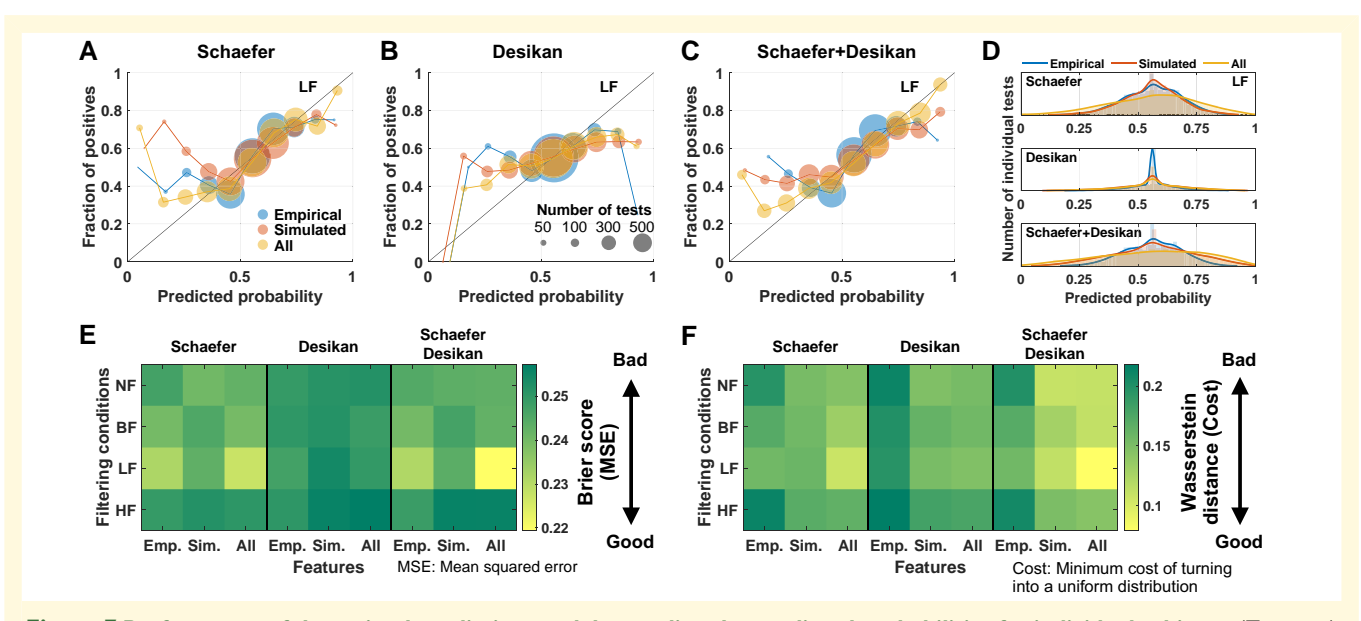


Figure 7 Performance of the trained prediction model regarding the predicted probabilities for individual subjects. (Top row) Plots of the probability calibrations from 5800 predictions for (A) the Schaefer atlas, (B) Desikan–Killiany atlas, and (C) multiple atlases, where the fraction of true positives is plotted versus the probability of them predicted by the trained model for individual subjects. The sizes of the circles indicate the number of individual subject tests for the three considered feature conditions as indicated in the legend in plot (A). (D) Histograms of the predicted probabilities (5800 predictions) for each feature condition, as indicated in the legend. The case of the LF band-pass filtering condition is illustrated in plots (A–D). (E) Table of the Brier scores (mean-squared error to the correct classes) for all considered filtering and feature conditions. (F) Tables of the Wasserstein distances between distributions of predicted probabilities and a uniform distribution for all conditions. Desikan–Killiany; Emp., empirical features; Sim., simulated features; All, empirical and simulated features.

validation. <sup>6,30,35,79</sup> In this respect, we investigated how temporal filtering of BOLD signals and brain parcellation influence empirical and simulated results regarding model fitting, group difference and prediction performance. Based on our results, we can conclude that the resting-state whole-brain simulations with appropriate data processing and model validation reflect personal traits of individual subjects, which may contribute to disease classification based on the whole-brain connectivity relationships with potential relevance in medicine.

# Effect of temporal filtering on model fitting and prediction

The effect of temporal filtering on functional MRI has been the focus of neuroimaging research for a long time. 80-83 One related study considered different temporal filters for MRI data processing and reported distinguishable BOLD dynamics in task-driven and resting-state brain activity

between low and high-frequency band-pass filtering.<sup>38</sup> Furthermore, temporal filtering can influence the classification performance for patients with Alzheimer's disease as compared across several low- and high-band-pass filtering conditions.<sup>39</sup> In this study, we found that the neuroimaging model fitting resulted in significantly different distributions of the maximal GoF values for individual subjects under different filtering conditions. Furthermore, the empirical structure-function connectivity relationship and the maximal GoF values of the neuroimaging model fitting were diminishing for the narrower filtering bands (Supplementary Fig. 4).

Another study investigated Parkinson's disease classification via machine learning on brain networks derived from the empirical resting-state FC with a high pass temporal filtering (> 0.01 Hz) of BOLD signals,<sup>36</sup> which corresponds to the case of the NF condition in our study. According to our prediction results, we suggest to consider the low-frequency band-pass filtering, i.e. the LF condition, which

can improve the differentiation and classification of Parkinson's disease also for the case when only empirical features are used.

An appropriate selection of the filtering condition (broador narrow-, high- or low-frequency band) appears to be important for the prediction performance, as reflected by several integrative measures considered in this study. In particular, a detailed evaluation of individual tests indicates that selecting a proper band-pass filter for the empirical and simulated BOLD signals can improve the prediction performance (Figs. 6 and 7).

In a broader perspective, changing parameter values or algorithms in a data processing pipeline can affect empirical results such as structural and functional connectivities, which in turn influence simulation results. In previous studies, for instance, we reported the impact of data processing on simulated results by whole-brain dynamical modelling: WBT densities, 30 region granularities, 6 parcellation schemes, 6,30,79,84 whole-brain simulation models 6,79,84 and model fitting approaches.<sup>6,30</sup> In the current study, we showed that applying temporal filtering to BOLD signals and using different brain parcellations and their combinations, as well as the neuroimaging and behavioural types of model fitting, can impact empirical and simulated results and their classification performance. Subsequently, we therefore investigated the impact of the considered parameter conditions of the data processing and model simulation on classification performance. By doing so, the conditional pipeline, which gives the highest performance, can be considered as contributing to the extent of the data and model personalization, which is important for subject classification based on clinical or behavioural data and their simulations.

# **Biophysical interpretation of model** parameters

Under the assumption that the resting-state brain activity is governed by a complex dynamical system, we can interpret the optimal model parameters of the neuroimaging model fitting as parameters of that system with potential neuroscientific/physical meaning. Since the optimal parameters were determined by distinct model validations, they can differ when a given model fitting approach changes as observed in our previous studies<sup>6,30</sup> and demonstrated by the results in the current study (Fig. 4C–D). Furthermore, the parcellations also impact on the locations of the optimal parameters. For instance, the optimal global coupling parameters derived from the behavioural model fitting suggest weaker optimal couplings than those from the neuroimaging model fitting for the Schaefer atlas (Fig. 4C). On the other hand, the situation for the Desikan–Killiany atlas is opposite (Fig. 4D).

In our model, we used the reconstructed PLs of the tractography streamlines in the white matter, which approximate the actual lengths of the anatomical axonal connections in the brain. The considered model simulates the electrical activity of the excitatory and inhibitory neuronal populations in the brain regions, as reflected by the dynamics of the

respective PSP signals. We can thus evaluate and interpret the optimal model parameters for the propagation of the simulated electrical signals (EPSP) along the brain pathways. We, in particular, found that the neuroimaging model fitting resulted in the optimal delay of the signal propagation in the electrophysiologically plausible range<sup>78</sup> (Fig. 3D and H). This confirms the applicability of the used dynamical model for simulating brain dynamics. Furthermore, the optimal delay of the behavioural model fitting obtained from repeated subsampling for different subject configurations is located in the same biologically reasonable range as well, which validates the behavioural model fit (Fig. 4C-D). Further parameters of the considered model and the simulated electrical PSP signals (Table 2) may have biologically plausible interpretations and ranges. Here we may mention, for example, the excitation-inhibition balance of the intra-regional coupling or the time constants responsible for controlling slow or fast oscillations of electrical neuronal activity.

In Parkinson's disease research, a neural model generating such oscillations in a certain frequency range is essential to engaging the pathological neural activity during rest. Previous studies reported that the resting-state corticocortical FC of Parkinson's disease patients changed in the 8-10 Hz range (in the alpha-rhythm) for early-stage and moderately advanced Parkinson's disease patients<sup>85</sup> and cortico-cortical coupling for oscillations between 10 and 35 Hz correlated with the severity of Parkinson's disease in the electroencephalogram study.86 High oscillatory synchrony in the basal ganglia at frequencies of 8-35 Hz was also associated with Parkinson's disease based on spectral power changes between off- and on-drug (levodopa dose). 87 With this respect, we may also investigate the relationship between frequencies of neural activity and models by varying the scale factor R of the current whole-brain dynamical model.

#### **Exploring parameter landscapes**

The neuroimaging model fitting is a well-established model validation as though maximizing GoF values of the model is the main objective of the model validation. Nevertheless, brain dynamics for non-optimal model parameters may also provide additional useful properties. They can contribute to the application of the dynamical models to analyse the brain and behaviour. In particular, brain modelling with virtual brains or in silico models for brain abnormalities has been used for clinical purposes. 26-28 To this end, we explored the parameter landscapes of GoF values and searched for parameter points that provide optimal GoF values to effectively answer the current research question. As we reported in the results, there exist hotspots of the densely located optimal model parameters, where either neuroimaging or behavioural model fitting is the most effective, although these hotspots may not coincide (Fig. 4C-D, the distributions in blue and orange). This should be linked to the definition of the atlas and, hence, regions. We also observed an impact of brain parcellations on the distributions of the optimal parameters. 6,30,79,84 A detailed investigation of this phenomenon will require considering more parcellation schemes to systematically describe their influence on the modelling results, as we already initiated in our previous studies. 6,30,79,84 Therefore, a systematic exploration of parameter landscapes allows us to find proper model parameters for a given purpose, which may be different in locations and other properties from one modelling condition and research question to another. Accordingly, we conclude that exploring parameter landscapes of the whole-brain dynamical models using behavioural/phenotypical measures might reveal optimal model parameters best suited for research goals related to inter-individual variability and prediction approaches.

# Classification of Parkinsonian patients

In this study, we did not aim at obtaining the highest prediction accuracy, which might have required extensive testing of many simulation and prediction conditions, feature spaces, and learning algorithms. Nevertheless, the obtained prediction performance (65.2% as median accuracy using empirical features) is comparable with that reported, for example, in the study of Plaschke *et al.*<sup>36</sup> which had a median accuracy of 65.5% over considered brain networks.

When we considered the simulated data for Parkinson's disease classification, the features from the neuroimaging model fitting had much lower performance in most considered cases as compared with the features from the behavioural model fitting (Supplementary Fig. 8). Therefore, we suggest that the behavioural model fitting can be used to validate the model against behavioural data for probing the simulated whole-brain dynamics to improve the model correspondence to phenotypical characteristics of subjects and prediction results. Such an approach may be of crucial importance in clinical research and the reported results showed promising confirmations.

In this study, we also explored the impact of a few data processing choices and model simulation on the differentiation and prediction performance. For example, composing predictive features including empirical and simulated connectomes from multiple brain atlases can provide complementary features leading to even better prediction performance (Supplementary Fig. 7). We further showed that also filtering conditions of empirical and simulated BOLD signals can play an important role in model validation and subject classification, where in particular, prediction specificity may vary significantly across filtering conditions as well as the number of false positives of the trained model can be reduced by appropriate filtering (Fig. 6).

Modern neuroimaging research dedicated to prediction analysis and based on machine learning techniques has shown enhanced performance for clinical data and in radiology in particular.<sup>67,88</sup> Those predictive results and developed approaches have faced the issue of translation of their

analysis and interpretation of the obtained outcomes to clinical application.<sup>89</sup> In this respect, the current study illustrated the characteristics of individual prediction probabilities to bridge the gap between modelling and prediction results and their translation for diagnosis in clinical research. The analysis included in the present study explored the calibration of the predicted probabilities for individual subjects and provided additional reliable information for the interpretation of the classification results. This can be achieved when the prediction probabilities are considered at the level of individual subjects, for example, when new, unseen patients are tested for diagnostic purposes. Furthermore, the discussed probability analysis delivered additional evidence that the whole-brain simulation results can be useful for complementing empirical data for prediction and classification in clinical research. Consequently, involving the whole-brain dynamical models in the training of machine learning models can improve individual prediction, which can potentially help a clinician better gauge a diagnosis during the examination of individual patients.

#### **Future work**

For further studies, other phenotypical properties can be used for the behavioural model fitting, for instance, age or sex. Of course, cognitive or clinical scores such as the Montreal Cognitive Assessment, Mattis dementia rating scales and the unified Parkinson's disease rating scales are also applicable. The suggested approach to behavioural model fitting is similar to the brain mapping of various behavioural or phenotypic measures on the cortical surface and can thus be generalized. In other words, we can map the parameter space using cognitive or clinical scores, which can be referred to as *phenotypical mapping* on the model parameter space like the behavioural model fitting that we introduced in the present study.

### **Summary**

We simulated whole-brain resting-state dynamics and calculated the relationships between structural and functional empirical and simulated connectomes for a variety of conditions and data processing, options including brain parcellation and temporal filtering of BOLD signals. We introduced the behavioural model fitting paradigm and found that the ensuing modelling results can lead to enhanced differentiation of disease and control groups and improved classification of Parkinsonian patients by machine learning approaches. Thus, the involvement of simulated connectomes, especially, in combination with empirical ones, is of great advantage, where the individual probabilities approach the ideal case as compared with the purely empirical feature space. We showed that band-pass filtering in the low-frequency band can have a beneficial effect on the prediction performance. On the other hand, the high-frequencies of the empirical and simulated BOLD signals should be considered with care and may not immediately be recommended for subject-level classification. In addition, we demonstrated that the prediction performance can differ for different or multiple brain parcellation schemes. Our findings can contribute to a better understanding of empirical and simulated whole-brain dynamics and their relationship to disease. They further suggest an avenue for application of the results of whole-brain simulations for cognitive or clinical investigation of interindividual differences and disease diagnosis.

### **Acknowledgements**

The authors greatly acknowledge the contribution of Dr. Christian Mathys, Dr. Martin Südmeyer and Dr. Christian Hartmann for the assessment of the Parkinson's disease data. The authors are also grateful to Shraddha Jain for the MRI data quality check. The authors gratefully acknowledge the computing time granted through JARA on the supercomputer JURECA at Forschungszentrum Jülich.

### **Funding**

This work was supported by the Portfolio Theme Supercomputing and Modeling for the Human Brain by the Helmholtz association (https://www.helmholtz.de/en), the Human Brain Project and the European Union's Horizon 2020 Research and Innovation Programme (https://cordis.europa.eu) under Grant Agreements 785907 (HBP SGA2), 945539 (HBP SGA3) and 826421 (VirtualBrainCloud). Open access publication was funded by the Deutsche Forschungsgemeinschaft (DFG, German Research Foundation)—491111487. The funders had no role in study design, data collection and analysis, decision to publish or preparation of the manuscript.

### **Competing interests**

The authors report no competing interests.

### **Supplementary Material**

Supplementary material is available at *Brain Communications* online.

### **Data availability**

The raw empirical data used in this study are not immediately available for public sharing because the given informed consent of the included patients did not include public sharing. The simulated data that support the findings of this study are available from the corresponding author upon a reasonable request.

### References

- Park HJ, Friston K. Structural and functional brain networks: From connections to cognition. Science. 2013;342(6158):1238411.
- Greicius MD, Supekar K, Menon V, Dougherty RF. Resting-state functional connectivity reflects structural connectivity in the default mode network. *Cereb Cortex*. 2009;19(1):72-78.
- 3. van den Heuvel MP, Mandl RC, Kahn RS, Hulshoff Pol HE. Functionally linked resting-state networks reflect the underlying structural connectivity architecture of the human brain. *Hum Brain Mapp.* 2009;30(10):3127-3141.
- van den Heuvel MP, Sporns O, Collin G, et al. Abnormal rich club organization and functional brain dynamics in schizophrenia. JAMA Psychiatry. 2013;70(8):783-792.
- Batista-Garcia-Ramo K, Fernandez-Verdecia CI. What we know about the brain structure-function relationship. *Behav Sci (Basel)*. 2018;8(4):39.
- Popovych OV, Jung K, Manos T, et al. Inter-subject and interparcellation variability of resting-state whole-brain dynamical modeling. NeuroImage. 2021;236:118201.
- Gu Z, Jamison KW, Sabuncu MR, Kuceyeski A. Heritability and interindividual variability of regional structure-function coupling. *Nat Commun.* 2021;12(1):4894.
- 8. Zamani Esfahlani F, Faskowitz J, Slack J, Misic B, Betzel RF. Local structure-function relationships in human brain networks across the lifespan. *Nat Commun.* 2022;13(1):2053.
- Finn ES, Shen X, Scheinost D, et al. Functional connectome fingerprinting: Identifying individuals using patterns of brain connectivity. Nat Neurosci. 2015;18(11):1664-1671.
- Cocchi L, Harding IH, Lord A, Pantelis C, Yucel M, Zalesky A. Disruption of structure-function coupling in the schizophrenia connectome. *Neuroimage Clin*. 2014;4:779-787.
- Wirsich J, Perry A, Ridley B, et al. Whole-brain analytic measures of network communication reveal increased structure-function correlation in right temporal lobe epilepsy. Neuroimage Clin. 2016;11: 707-718.
- Zarkali A, McColgan P, Leyland LA, Lees AJ, Rees G, Weil RS. Organisational and neuromodulatory underpinnings of structuralfunctional connectivity decoupling in patients with Parkinson's disease. Commun Biol. 2021;4(1):86.
- 13. Honey CJ, Sporns O, Cammoun L, et al. Predicting human restingstate functional connectivity from structural connectivity. Proc Natl Acad Sci U S A. 2009;106(6):2035-2040.
- 14. Deco G, Tononi G, Boly M, Kringelbach ML. Rethinking segregation and integration: Contributions of whole-brain modelling. *Nat Rev Neurosci*. 2015;16(7):430-439.
- Naskar A, Vattikonda A, Deco G, Roy D, Banerjee A. Multiscale dynamic mean field (MDMF) model relates resting-state brain dynamics with local cortical excitatory-inhibitory neurotransmitter homeostasis. *Netw Neurosci*. 2021;5(3):757-782.
- 16. Cabral J, Kringelbach ML, Deco G. Functional graph alterations in schizophrenia: A result from a global anatomic decoupling? *Pharmacopsychiatry*. 2012;45(Suppl 1):S57-S64.
- Cabral J, Fernandes HM, Van Hartevelt TJ, James AC, Kringelbach ML, Deco G. Structural connectivity in schizophrenia and its impact on the dynamics of spontaneous functional networks. *Chaos*. 2013; 23(4):046111.
- 18. Yang GJ, Murray JD, Repovs G, et al. Altered global brain signal in schizophrenia. Proc Natl Acad Sci USA. 2014;111(20):7438-7443.
- 19. Anticevic A, Hu X, Xiao Y, et al. Early-course unmedicated schizophrenia patients exhibit elevated prefrontal connectivity associated with longitudinal change. *J Neurosci*. 2015;35(1):267-286.
- Zimmermann J, Perry A, Breakspear M, et al. Differentiation of Alzheimer's disease based on local and global parameters in personalized virtual brain models. Neuroimage Clin. 2018;19:240-251.
- 21. van Hartevelt TJ, Cabral J, Deco G, et al. Neural plasticity in human brain connectivity: The effects of long term deep brain stimulation

- of the subthalamic nucleus in Parkinson's disease. *Plos One*. 2014; 9(1):e86496.
- Saenger VM, Kahan J, Foltynie T, et al. Uncovering the underlying mechanisms and whole-brain dynamics of deep brain stimulation for Parkinson's disease. Sci Rep. 2017;7(1):9882.
- Falcon MI, Riley JD, Jirsa V, McIntosh AR, Chen EE, Solodkin A. Functional mechanisms of recovery after chronic stroke: Modeling with the virtual brain. eNeuro. 2016;3(2):ENEURO.0158– 15.2016.
- 24. Deco G, Kringelbach ML, Jirsa VK, Ritter P. The dynamics of resting fluctuations in the brain: Metastability and its dynamical cortical core. *Sci Rep.* 2017;7(1):3095.
- Popovych OV, Tass PA. Control of abnormal synchronization in neurological disorders. Front Neurol. 2014;5:268.
- Popovych OV, Tass PA. Adaptive delivery of continuous and delayed feedback deep brain stimulation—a computational study. Sci Rep. 2019;9(1):10585.
- Aerts H, Schirner M, Dhollander T, et al. Modeling brain dynamics after tumor resection using the virtual brain. NeuroImage. 2020; 213:116738.
- 28. An S, Fousek J, Kiss ZHT, et al. High-resolution virtual brain modeling personalizes deep brain stimulation for treatment-resistant depression: Spatiotemporal response characteristics following stimulation of neural fiber pathways. NeuroImage. 2022;249: 118848.
- 29. Cabral J, Vidaurre D, Marques P, et al. Cognitive performance in healthy older adults relates to spontaneous switching between states of functional connectivity during rest. *Sci Rep.* 2017;7(1):5135.
- Jung K, Eickhoff SB, Popovych OV. Tractography density affects whole-brain structural architecture and resting-state dynamical modeling. *NeuroImage*. 2021;237:118176.
- Varikuti DP, Hoffstaedter F, Genon S, Schwender H, Reid AT, Eickhoff SB. Resting-state test-retest reliability of a priori defined canonical networks over different preprocessing steps. *Brain Struct Funct*. 2017;222(3):1447-1468.
- 32. Botvinik-Nezer R, Holzmeister F, Camerer CF, et al. Variability in the analysis of a single neuroimaging dataset by many teams. *Nature*. 2020;582(7810):84-88.
- 33. Bhagwat N, Barry A, Dickie EW, *et al.* Understanding the impact of preprocessing pipelines on neuroimaging cortical surface analyses. *Gigascience*. 2021;10(1):giaa155.
- Borrelli P, Cavaliere C, Salvatore M, Jovicich J, Aiello M. Structural brain network reproducibility: Influence of different diffusion acquisition and tractography reconstruction schemes on graph metrics. *Brain Connect*. 2022;12(8):754-767.
- 35. Popovych OV, Manos T, Hoffstaedter F, Eickhoff SB. What can computational models contribute to neuroimaging data analytics? *Front Syst Neurosci.* 2019;12:68.
- Plaschke RN, Cieslik EC, Muller VI, et al. On the integrity of functional brain networks in schizophrenia, Parkinson's disease, and advanced age: Evidence from connectivity-based single-subject classification. Hum Brain Mapp. 2017;38(12):5845-5858.
- Rubbert C, Mathys C, Jockwitz C, et al. Machine-learning identifies Parkinson's disease patients based on resting-state betweennetwork functional connectivity. Br J Radiol. 2019;92(1101): 20180886.
- 38. Baria AT, Baliki MN, Parrish T, Apkarian AV. Anatomical and functional assemblies of brain BOLD oscillations. *J Neurosci*. 2011;31(21):7910-7919.
- Wee CY, Yap PT, Denny K, et al. Resting-state multi-spectrum functional connectivity networks for identification of MCI patients. Plos One. 2012;7(5):e37828.
- Hou Y, Wu X, Hallett M, Chan P, Wu T. Frequency-dependent neural activity in Parkinson's disease. *Hum Brain Mapp*. 2014;35-(12):5815-5833.
- Schaefer A, Kong R, Gordon EM, et al. Local-global parcellation of the human cerebral cortex from intrinsic functional connectivity MRI. Cereb Cortex. 2018;28(9):3095-3114.

- 42. Desikan RS, Segonne F, Fischl B, et al. An automated labeling system for subdividing the human cerebral cortex on MRI scans into gyral based regions of interest. NeuroImage. 2006;31(3): 968-980.
- 43. Lopes da Silva FH, Hoeks A, Smits H, Zetterberg LH. Model of brain rhythmic activity. The alpha-rhythm of the thalamus. *Kybernetik*. 1974;15(1):27-37.
- 44. Jansen BH, Rit VG. Electroencephalogram and visual evoked potential generation in a mathematical model of coupled cortical columns. *Biol Cybern*. 1995;73(4):357-366.
- 45. Mathys C, Caspers J, Langner R, et al. Functional connectivity differences of the subthalamic nucleus related to Parkinson's disease. Hum Brain Mapp. 2016;37(3):1235-1253.
- Caspers J, Mathys C, Hoffstaedter F, et al. Differential functional connectivity alterations of two subdivisions within the right dlPFC in Parkinson's disease. Front Hum Neurosci. 2017;11:288.
- 47. Dale AM, Fischl B, Sereno MI. Cortical surface-based analysis. I. Segmentation and surface reconstruction. *NeuroImage*. 1999;9(2):179-194.
- 48. Smith SM, Jenkinson M, Woolrich MW, *et al.* Advances in functional and structural MR image analysis and implementation as FSL. *NeuroImage*. 2004;23(Suppl 1):S208-S219.
- 49. Tustison NJ, Avants BB, Cook PA, et al. N4ITK: Improved N3 bias correction. IEEE Trans Med Imaging. 2010;29(6):1310-1320.
- Tournier JD, Smith R, Raffelt D, et al. MRtrix3: A fast, flexible and open software framework for medical image processing and visualisation. NeuroImage. 2019;202:116137.
- Cox RW. AFNI: Software for analysis and visualization of functional magnetic resonance neuroimages. Comput Biomed Res. 1996; 29(3):162-173.
- 52. Fischl B, van der Kouwe A, Destrieux C, et al. Automatically parcellating the human cerebral cortex. *Cereb Cortex*. 2004;14(1): 11-22.
- Jeurissen B, Tournier JD, Dhollander T, Connelly A, Sijbers J. Multi-tissue constrained spherical deconvolution for improved analysis of multi-shell diffusion MRI data. *NeuroImage*. 2014;103: 411-426.
- Tournier JD, Calamante F, Connelly A. Improved probabilistic streamlines tractography by 2nd order integration over fibre orientation distributions. *Proc Int Soc Magn Reson Med*. 2010;18:1670.
- Virtanen P, Gommers R, Oliphant TE, et al. Scipy 1.0: Fundamental algorithms for scientific computing in python. Nat Methods. 2020; 17(3):261-272.
- van der Walt S, Colbert SC, Varoquaux G. The NumPy array: A structure for efficient numerical computation. Comput Sci Eng. 2011;13(2):22-30.
- 57. Moran R, Pinotsis DA, Friston K. Neural masses and fields in dynamic causal modeling. Front Comput Neurosci. 2013;7:57.
- Havlicek M, Roebroeck A, Friston K, Gardumi A, Ivanov D, Uludag K. Physiologically informed dynamic causal modeling of fMRI data. *NeuroImage*. 2015;122:355-372.
- Buxton RB, Wong EC, Frank LR. Dynamics of blood flow and oxygenation changes during brain activation: The balloon model. *Magn Reson Med.* 1998;39(6):855-864.
- Friston KJ, Harrison L, Penny W. Dynamic causal modelling. NeuroImage. 2003;19(4):1273-1302.
- 61. Rosenthal R. Parametric measures of effect size. In: Cooper H and Hedges L, eds. *The handbook of research synthesis*. Russell Sage Foundation; 1994:621(2):231-244.
- 62. Worsley KJ, Evans AC, Marrett S, Neelin P. A three-dimensional statistical analysis for CBF activation studies in human brain. *J Cereb Blood Flow Metab*. 1992;12(6):900-918.
- Ashburner J, Friston KJ, Penny W. Human brain function. 2nd edn. Academic Press; 2003.
- 64. Shimizu Y, Yoshimoto J, Toki S, et al. Toward probabilistic diagnosis and understanding of depression based on functional MRI data analysis with logistic group LASSO. Plos One. 2015;10(5): e0123524.

- Schouten TM, Koini M, Vos F, et al. Individual classification of Alzheimer's disease with diffusion magnetic resonance imaging. NeuroImage. 2017;152:476-481.
- 66. Priya S, Liu Y, Ward C, *et al.* Machine learning based differentiation of glioblastoma from brain metastasis using MRI derived radiomics. *Sci Rep.* 2021;11(1):10478.
- 67. Mei J, Desrosiers C, Frasnelli J. Machine learning for the diagnosis of Parkinson's disease: A review of literature. *Front Aging Neurosci*. 2021:13:633752.
- 68. Tibshirani R. Regression shrinkage and selection via the lasso. *J R Stat Soc Ser B (Methodological)*. 1996;58(1):267-288.
- Hastie T, Tibshirani R, Friedman J. The elements of statistical learning. 2nd edn. Springer; 2009.
- 70. Tanner CM, Goldman SM. Epidemiology of Parkinson's disease. *Neurol Clin.* 1996;14(2):317-335.
- 71. de Lau LML, Breteler MMB. Epidemiology of Parkinson's disease. *Lancet Neurol*. 2006;5(6):525-535.
- 72. More S, Eickhoff SB, Caspers J, Patil KR. Confound removal and normalization in practice: A neuroimaging based sex prediction case study. In: Dong Y, Ifrim G, Mladenić D, Saunders C, Van Hoecke S, eds. *Machine Learning and Knowledge Discovery in Databases. Applied Data Science and Demo Track: European Conference, ECML PKDD 2020*, Ghent, Belgium, September 14–18, 2020. Lecture Notes in Computer Science, Vol 12461. Springer; 2021:3-18.
- Vabalas A, Gowen E, Poliakoff E, Casson AJ. Machine learning algorithm validation with a limited sample size. *Plos One*. 2019;14-(11):e0224365.
- 74. Fawcett T. An introduction to ROC analysis. *Pattern Recognit Lett.* 2006;27(8):861-874.
- 75. Kompa B, Snoek J, Beam AL. Second opinion needed: Communicating uncertainty in medical machine learning. NPJ Digit Med. 2021;4(1):4.
- Brier GW. Verification of forecasts expressed in terms of probability. Mon Weather Rev. 1950;78(1):1-3.
- 77. Kantorovich LV. Mathematical methods of organizing and planning production. *Manage Sci.* 1960;6(4):366-422.
- 78. Caminiti R, Carducci F, Piervincenzi C, et al. Diameter, length, speed, and conduction delay of callosal axons in macaque monkeys and humans: Comparing data from histology and magnetic

- resonance imaging diffusion tractography. *J Neurosci*. 2013;33-(36):14501-14511.
- Domhof JWM, Jung K, Eickhoff SB, Popovych OV. Parcellation-induced variation of empirical and simulated brain connectomes at group and subject levels. *Netw Neurosci.* 2021; 5(3):798-830.
- Friston KJ, Josephs O, Zarahn E, Holmes AP, Rouquette S, Poline J. To smooth or not to smooth? Bias and efficiency in fMRI time-series analysis. *NeuroImage*. 2000;12(2):196-208.
- 81. Zuo XN, Di Martino A, Kelly C, et al. The oscillating brain: Complex and reliable. NeuroImage. 2010;49(2):1432-1445.
- Boubela RN, Kalcher K, Huf W, Kronnerwetter C, Filzmoser P, Moser E. Beyond noise: Using temporal ICA to extract meaningful information from high-frequency fMRI signal fluctuations during rest. Front Hum Neurosci. 2013;7:168.
- 83. Vergara VM, Mayer AR, Damaraju E, Hutchison K, Calhoun VD. The effect of preprocessing pipelines in subject classification and detection of abnormal resting state functional network connectivity using group ICA. *NeuroImage*. 2017;145(Pt B): 365-376.
- 84. Domhof JWM, Eickhoff SB, Popovych OV. Reliability and subject specificity of personalized whole-brain dynamical models. *NeuroImage*. 2022;257:119321.
- 85. Stoffers D, Bosboom JL, Deijen JB, Wolters E, Stam CJ, Berendse HW. Increased cortico-cortical functional connectivity in early-stage Parkinson's disease: An MEG study. *NeuroImage*. 2008; 41(2):212-222.
- Silberstein P, Pogosyan A, Kuhn AA, et al. Cortico-cortical coupling in Parkinson's disease and its modulation by therapy. Brain. 2005; 128(Pt 6):1277-1291.
- 87. Kuhn AA, Tsui A, Aziz T, *et al.* Pathological synchronisation in the subthalamic nucleus of patients with Parkinson's disease relates to both bradykinesia and rigidity. *Exp Neurol.* 2009;215(2): 380-387.
- 88. Burgos N, Colliot O. Machine learning for classification and prediction of brain diseases: Recent advances and upcoming challenges. *Curr Opin Neurol.* 2020;33(4):439-450.
- 89. Caspers J. Translation of predictive modeling and AI into clinics: A question of trust. *Eur Radiol*. 2021;31(7):4947-4948.